

Silver–Cytosine–Polyoxometalate Assemblies: Assessing the Role of Polyoxometalates in Constructing Ag–DNA Suprastructures

Rachelle M. Smith, Ian Colliard, Mehran Amiri, Miguel A. Galindo,* and May Nyman*



Cite This: *Cryst. Growth Des.* 2022, 22, 2294–2306



Read Online

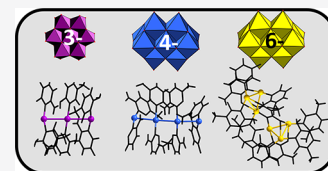
ACCESS |

Metrics & More

Article Recommendations

Supporting Information

ABSTRACT: Engineered DNA–metal complexes and superstructures have been shown to combine superior control of DNA helices and metal–metal interactions to create nanowires with unique luminescence and conductivity properties. Recently, their solid-state characterization reveals polymerization of the metal–DNA helices, leading to a one-dimensional Ag–DNA array. Here, we investigate the potential of polyoxometalates (POMs) to connect and join metal–DNA complexes to disrupt polymerization and control the dimensionality and nuclearity of Ag chains and clusters. We have used $[Ag(^m\text{cytosine})_2]^+$ complexes ($^m\text{cytosine}$ = 1-methyl-cytosine) as inexpensive and well-known models for metal–DNA complexes, to assemble and structurally characterize (via single-crystal X-ray diffraction) five Ag– $^m\text{cytosine}$ –POM lattices: (1) three featuring the $[CrMo_6(OH)_6O_{18}]^{3-}$ Anderson POM, (2) one with decavanadate ($[M_{10}O_{28}]^{6-}$; M = V or Nb). Both covalent and noncovalent interactions drive the crystallization of the observed Ag– $^m\text{cytosine}$ –POM assemblies, including the targeted Ag–POM bonding. Noncovalent associations include π – π interactions of Ag-bound and unbound $^m\text{cytosine}$ ligands, Ag–Ag argentophilic interactions, and H-bonding between POMs and $^m\text{cytosine}$. These structures reveal that we can influence the $[Ag^+]_n$ nuclearity by the charge and protonation state of the POM, while the basicity of the POM influences Ag–POM bonding. In addition, we isolate an unprecedented binuclear silver-mediated cytosine pair adopting a Watson–Crick conformation.



INTRODUCTION

Ag^+ is a unique cation to construct hybrid assemblies from molecular building blocks via argentophilic interactions, i.e., Ag^+ – Ag^+ association. In this regard, an important growing field is the use of DNA to construct nanomaterials that could exploit Ag^+ – Ag^+ interactions to form predictable shapes, i.e., nanowires and DNA-templated silver nanoclusters.^{1,2} The structure of DNA is well-known and predictable, and its assembly is based on hydrogen bonding and π – π stacking of the base pairs to create double helices with customizable shapes.³ Depending on the structure of the DNA, the distance between the base pairs along the double helix is between 2.6 and 3.5 Å, a distance comparable to that of Ag^+ – Ag^+ interactions.⁴ Still, controlling the position and stoichiometry of Ag^+ in the helix is not a trivial task. A smart strategy to overcome this challenge is demonstrated with the use of the so-called “metal-mediated base pairs”, in which Watson–Crick hydrogen bonds are substituted by coordination bonds to central metal ions.⁵ This approach has been used to assemble different Ag–DNA hybrids. Those containing a continuous Ag^+ chain running through the center of the double helix^{6–9} have potential application in nanotechnology, i.e., nanoelectronics.¹⁰ Remarkably, the crystal structure of an uninterrupted one-dimensional Ag–DNA system (Ag–Ag distance of 3.2–3.4 Å) was obtained using a dodecamer duplex with an overhanging base that allowed the polymerization of the dodecamers (Figure 1a).¹¹

Although metal-mediated base pairs can be prepared using canonical or noncanonical bases, cytosine has an extraordinary

tendency to form silver-mediated cytosine pairs and, therefore, has been the subject of several studies. Cytosine and its N1-alkylated derivatives show metal binding preference toward the imino-N3 position and keto-O2 (Figure 1c).¹² In this regard, different silver-mediated cytosine pairs of types $[Ag(N3\text{-cytosine})_2]^+$ and $[Ag(N3\text{-O}_2\text{-cytosine})_2]^+$ (cytosine = cytosine derivatives) have been reported and studied, both inside and outside DNA molecules. They can also form one-dimensional silver coordination polymers (Figure 1b),^{13–16} similar to DNA.

We are investigating polyoxometalates (POMs, molecular metal-oxo clusters composed of V^V , Nb^V , Ta^V , Mo^{VI} , or W^{VI})¹⁷ as a yet unexplored strategy to connect and join Ag–DNA and Ag^+ –base complex helices that could lead to molecular networks for potential nanotechnology applications, i.e., assembly of molecular electronics or drug delivery systems. Ag^+ –base complex helices require an anionic charge balance that the POMs can provide, in addition to serving as nodes to tether and link isolated $[Ag]_n$ chains. Like DNA, POMs can have predictable and invariable molecular formulae and geometries that persist in solution due to doubly bonded oxo-ligands (known as the “yl”-oxo) passivating the cluster

Received: November 25, 2021

Revised: March 8, 2022

Published: March 21, 2022



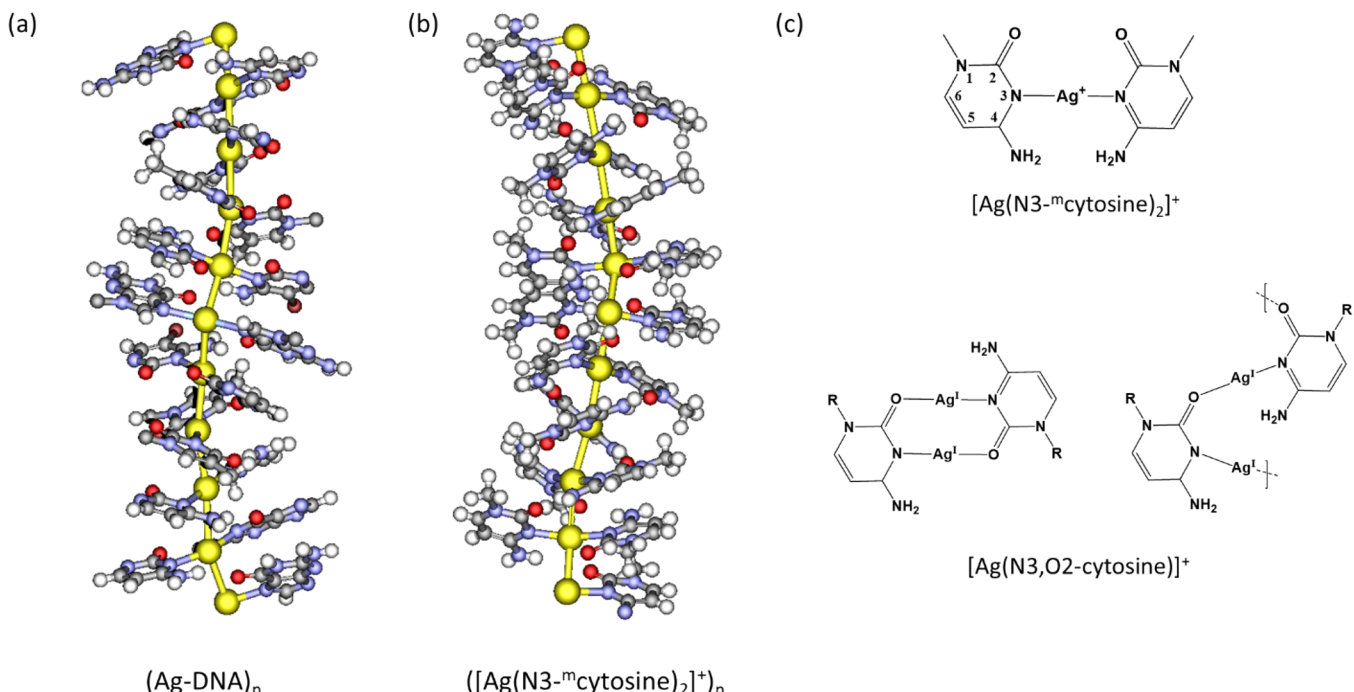


Figure 1. (a) Simplified structure of the Ag–DNA polymer previously published¹¹ (phosphate and 2'-deoxyribose units have been omitted for clarity). (b) Structure example of the $[\text{Ag}(\text{N}3\text{-}^m\text{cytosine})_2]^+$ polymer (analogous to DNA) previously reported.¹³ (c) Scheme showing different binding modes for the interaction between silver ions and cytosine derivatives (${}^m\text{cytosine} = 1\text{-methyl-cytosine}$). Atom color code: gray spheres are carbon, white spheres are hydrogen, blue spheres are nitrogen, red spheres are oxygen, and yellow spheres are silver.

surface and maintaining the cluster form without additional ligands. These stable clusters, unencumbered by organic ligation, can then be exploited as building blocks for hybrid materials that combine properties of the POM plus one or more additional molecular components. Emerging materials include inorganic frameworks, bioinorganic assemblies, metal–organic frameworks, and many more.^{18–26} POMs have also been used to isolate Ag^+ linear chains,²⁷ discrete clusters,^{28,29} and cages.³⁰ Luminescence and conductivity of the polynuclear Ag assemblies inspire applications of Ag–POM hybrid materials.^{23,31}

Here, we target the self-assembly of $[\text{Ag}({}^m\text{cytosine})_2]^+$ complexes (${}^m\text{cytosine} = 1\text{-methyl-cytosine}$) and POM crystalline lattices, to probe modes of Ag–base–POM interactions, determine the many potential roles of POMs in self-assembly processes, and predict Ag–DNA–POM interactions. As previously mentioned, $[\text{Ag}(\text{cytosine})_2]^+$ complexes are well-described in the literature and exhibit helices that are almost analogues to DNA (Figure 1).^{13–16,32} Additionally, several studies demonstrate the interaction of cytosine with POMs.^{33,34} Here, we describe five Ag– ${}^m\text{cytosine}$ –POM crystalline assemblies including the following:

- (1) $(\text{Ag}({}^m\text{cytosine})_2)_3 \cdot [\text{CrMo}_6(\text{OH})_6\text{O}_{18}] \cdot 17\text{H}_2\text{O}$, (${}^m\text{cytosine}$) ($\text{Ag}_3\text{-CrMo}_6\text{-1}$)
- (2) $(\text{Ag}({}^m\text{cytosine})_2)_3 \cdot [\text{CrMo}_6(\text{OH})_6\text{O}_{18}] \cdot 14\text{H}_2\text{O}, 2\text{-}({}^m\text{cytosine})$ ($\text{Ag}_3\text{-CrMo}_6\text{-2}$)
- (3) $(\text{Ag}({}^m\text{cytosine})_2)_2 \cdot [(\text{H}_{0.5})^m\text{cytosine}]_2 [\text{CrMo}_6(\text{OH})_6\text{O}_{18}] \cdot 17\text{H}_2\text{O}$ ($\text{Ag}_2\text{-CrMo}_6$)
- (4) $(\text{Ag}({}^m\text{cytosine})_2)_4 [\text{H}_2\text{V}_{10}\text{O}_{28}] \cdot 14\text{H}_2\text{O}$ ($\text{Ag}_4\text{-V}_{10}$)
- (5) $(\text{Ag}_3({}^m\text{cytosine})_5)_2 \cdot [\text{Nb}_{10}\text{O}_{28}] \cdot 8\text{H}_2\text{O}$ ($\text{Ag}_6\text{-Nb}_{10}$)

The Anderson–Evans POM¹⁸ was chosen for this study due to its great compositional flexibility and its prior use in protein

crystallization and structure elucidation.^{18,35} With the general formula $[\text{XM}_6\text{O}_{24}]^{n-}$ ($\text{M} = \text{Mo}^{\text{VI}}$ or W^{VI} ; $\text{X} = \text{heterometal}$, $n = 2–8$ depending on the charge of X), a small flat architecture, and a wide pH stability range, this POM has also been exploited in materials design via functionalization.^{36–38} Its protonated faces (up to six protons, three on each face) provide an opportunity for supramolecular assembly via H-bonding. Similarly, decavanadate, $[\text{H}_x\text{V}_{10}\text{O}_{28}]^{(x-6)}$ ($x = 2$ or 3), is small and stable, and its di- or triprotonated form also promotes intermolecular interactions, noted in both the solid state and in solution.^{39,40} Moreover, the biological function of vanadate species including decavanadate $[\text{H}_x\text{V}_{10}\text{O}_{28}]^{(x-6)}$ has been extensively investigated,^{34,41–47} inspiring its use in the current study. Additionally, several silver–POM assemblies have been described that feature decavanadate and the Anderson–Evans clusters, exhibiting various Ag–POM binding modes.^{48–50}

Of all the structures that we present here with V_{10} and CrMo_6 POMs, only $\text{Ag}_2\text{-CrMo}_6$, which forms as a minor phase, exhibits direct bonding between the $[\text{Ag}({}^m\text{cytosine})_2]^+$ complex and the POM, inspiring studies with more basic polyoxoniobates.⁵¹ Indeed, decaniobate, Nb_{10} , exhibits Ag–POM bonding in a rapidly precipitated and pure phase. Intriguingly, four of the five presented phases (all except $\text{Ag}_2\text{-CrMo}_6$) indicate that one major role of the POM in such assemblies is dictating the nuclearity of the Ag polynuclear chain or cluster. The rich variety of Ag– ${}^m\text{cytosine}$ –POM interactions demonstrated in this study, both coordinate covalent and noncovalent, suggests that POMs could play a key role in the next generation of metallo-DNA-based materials.

Table 1. Crystal Data and Structure Refinement for Ag-CrMo₆ Ag–Cytosine Compounds

	Ag ₂ -CrMo ₆ -2	Ag ₂ -CrMo ₆ -1
identification code	2102482	2102483
CCDC	C ₄₀ H ₇₈ Ag ₂ CrMo ₆ N ₂₄ O ₄₀	C ₈₀ H ₁₂₄ Ag ₂ Cr ₂ Mo ₁₂ N ₄₈ O ₉₄
empirical formula	2378.64	5004.76
formula weight	99.9(9)	105(6)
temperature/K		100(1)
crystal system	monoclinic	monoclinic
space group	P2 ₁ /c	C2/c
a/Å	11.18580(10)	24.1791(2)
b/Å	17.13200(10)	12.30630(10)
c/Å	19.83320(10)	28.7376(3)
$\alpha/^\circ$	90	90
$\beta/^\circ$	104.6110(10)	99.7160(10)
$\gamma/^\circ$	90	90
volume/Å ³	3677.82(5)	8428.37(13)
Z	2	2
ρ_{calc} (g/cm ³)	2.148	1.972
μ/mm^{-1}	14.425	14.430
F(000)	2352.0	4892.0
crystal size/mm ³	? × 0.02 × 0.01	0.3 × 0.3 × 0.1
radiation	Cu K α (λ = 1.54184)	Cu K α (λ = 1.54184)
2θ range for data collection/°	6.916–152.13	6.24–152.458
index ranges	$-9 \leq h \leq 14$, $-20 \leq k \leq 21$, and $-24 \leq l \leq 24$	$-30 \leq h \leq 30$, $-8 \leq k \leq 14$, and $-35 \leq l \leq 35$
reflections collected	26454	58472
independent reflections	7415 [$R_{\text{int}} = 0.0493$, $R_{\text{sigma}} = 0.0392$]	8597 [$R_{\text{int}} = 0.1035$, $R_{\text{sigma}} = 0.0419$]
data/restraints/parameters	7415/0/531	8597/0/544
goodness-of-fit on F^2	1.108	1.075
final R indexes [$I \geq 2\sigma(I)$]	$R_1 = 0.0363$, $wR_2 = 0.0982$	$R_1 = 0.0550$, $wR_2 = 0.1483$
final R indexes [all data]	$R_1 = 0.0403$, $wR_2 = 0.1087$	$R_1 = 0.0566$, $wR_2 = 0.1525$
largest diff. peak/hole (e Å ⁻³)	1.02/-1.51	1.55/-2.25

Table 2. Crystal Data and Structure Refinement for V₁₀ and Nb₁₀ Ag–Cytosine Compounds

identification code	Ag ₄ -V ₁₀	Ag ₆ -Nb ₁₀
CCDC	2102485	2103588
empirical formula	C ₄₀ H ₅₆ Ag ₄ N ₂₄ O ₃₆ V ₁₀	C ₅₀ H ₅₂ Ag ₆ N ₃₀ Nb ₁₀ O ₄₆
formula weight	2389.96	3385.53
temperature/K	99.9(9)	107(9)
crystal system	monoclinic	triclinic
space group	P2 ₁ /n	P ₁
a/Å	18.1213(3)	14.243(3)
b/Å	24.3220(3)	14.444(4)
c/Å	21.3476(3)	14.495(4)
α/°	90	115.07(2)
β/°	112.164(2)	109.45(2)
γ/°	90	102.96(2)
volume/Å ³	8713.6(2)	2302.2(11)
Z	4	1
ρ _{calc} (g/cm ³)	1.822	2.442
μ/mm ⁻¹	16.366	20.672
F(000)	4680.0	1622.0
crystal size/mm ³	0.07 × 0.01 × 0.01	0.02 × 0.01 × 0.009
radiation	Cu K α (λ = 1.54184)	Cu K α (λ = 1.54184)
2θ range for data collection/°	5.472–133.202	7.26–103.928
index ranges	-21 ≤ h ≤ 21, -28 ≤ k ≤ 28, and -20 ≤ l ≤ 25	-12 ≤ h ≤ 14, -14 ≤ k ≤ 13, and -14 ≤ l ≤ 14
reflections collected	108,992	4604
independent reflections	15,405 [$R_{\text{int}} = 0.0868$, $R_{\text{sigma}} = 0.0390$]	3196 [$R_{\text{int}} = 0.0958$, $R_{\text{sigma}} = 0.1573$]
data/restraints/parameters	15,405/0/1035	3196/1/316
goodness-of-fit on F^2	1.041	1.159
final R indexes [$I \geq 2\sigma(I)$]	$R_1 = 0.0680$, $wR_2 = 0.1933$	$R_1 = 0.1248$, $wR_2 = 0.3258$
final R indexes [all data]	$R_1 = 0.0738$, $wR_2 = 0.2003$	$R_1 = 0.1932$, $wR_2 = 0.3609$
largest diff. peak/hole (e Å ⁻³)	2.10/-1.00	3.34/-2.29

EXPERIMENTAL METHODS

Synthesis. Note: Silver salts were always contained in vials wrapped in foil to avoid light exposure, and all solutions and products were stored in dark cabinets.

Na₃[CrMo₆(OH)₆O₁₈]·8H₂O (CrMo₆). We synthesized CrMo₆ following a known literature procedure.⁵² Na₂MoO₄·2H₂O (0.352 mol, 72.5 g) was dissolved in water (300 mL), and the pH was adjusted to 4.5 using concentrated HNO₃. A second solution was prepared by dissolving Cr(NO₃)₃·9H₂O (0.84 mol, 20.0 g) in 20 mL of water. The two solutions were mixed in a 1 L bottle, which was then capped and let to sit at room temperature. Within one day, reddish-purple crystals started to form. After one week, the crystals were then vacuum filtered and washed multiple times with cold water. The collected precipitate was characterized by FT-IR (Figure S1) and PXRD to confirm the formation of CrMo₆ (yield of 45 g, ~50% based on molybdenum).

Na₆(V₁₀O₂₈)·16H₂O (V₁₀). V₁₀ was prepared by following a modified reported synthetic procedure.⁵³ NaVO₃ (0.025 mol, 3.0 g) was dissolved in water (100 mL). The solution was then adjusted to a pH of 4.8 using HCl (4 M) and filtered, and the pH was adjusted again to maintain a pH of 4.5. Ethanol was added to the solution to precipitate the orange microcrystals. The precipitate was then vacuum filtered and washed with ethanol. The collected precipitate was characterized by FT-IR (Figure S2) and PXRD to confirm the formation of Na₆(V₁₀O₂₈)·16H₂O (yield of ~2.8 g, 76% based on vanadium).

TMA₆[Nb₁₀O₂₈]·xH₂O. Decaniobate was prepared as prior described.⁵⁴ Briefly, hexaniobate, [(CH₃)₄N]₅H₃[Nb₆O₁₉], was first prepared.⁵⁵ Hexaniobate (0.004 mol, 5 g) was added to ethanol (50 mL) and stirred for 20 min, resulting in a white suspension. The mixture was then placed in a Paar reactor and heated at 140 °C for 18 h. The brown supernatant was discarded, and the white precipitate was vacuum filtered and washed with ethanol (50 mL) and dried in

air. The collected precipitate (600 g, 83% yield) was characterized by FT-IR (Figure S3) to confirm the formation of decaniobate.

[Ag(^mcytosine)₂](NO₃) Complex (AgC₂). For each reaction with a POM, a fresh stock solution of the ^mcytosine (0.22 mmol, 0.0275 g, 1.25 mL of water) and a stock solution of AgNO₃ (0.3 mmol, 0.05 g, 1.25 mL of water) were prepared. The silver complex was obtained by mixing 1.14 mL (200 μmol) of ^mcytosine stock solution with 1.08 mL (100 μmol) of AgNO₃ stock solution. The mixture was left to react with slow stirring at 50 °C for 1 h to form AgC₂ as a soluble species and used in subsequent reactions without isolation.

(Ag(^mcytosine)₂)₃·[CrMo₆(OH)₆O₁₈]·14H₂O, 2(^mcytosine)(Ag₃-CrMo₆-2), (Ag(^mcytosine)₂)₃·[CrMo₆(OH)₆O₁₈]·17H₂O, 2(^mcytosine) (Ag₃-CrMo₆-1), and (Ag(^mcytosine)₂)₂·[(H_{1-x})^mcytosine]₂·[CrMo₆(OH)₆O₁₈]·17H₂O (Ag₂-CrMo₆). A stock solution of the POM was prepared by dissolving CrMo₆ (0.2 mmol, 250 mg) in H₂O (10 mL). Then, 2.46 mL of the CrMo₆ solution was added to the freshly prepared AgC₂ solution. This gave a 2:1 AgC₂:CrMo₆ ratio. Immediately upon the combination of the two solutions, a light pink suspension formed. This was followed by the addition of H₂O (15.3 mL) to attempt to redissolve the precipitate, but the pink suspension persisted. The solution was centrifuged, and then, the powder was collected and dried in a vacuum oven overnight. The supernatant was placed in the dark, and single crystals suitable for X-ray diffraction formed within 15 h. The single-crystal X-ray diffraction measurements demonstrated the presence of the three titled compounds in a mixture of crystals. The quantity of crystals obtained was very small, and bulk characterization was performed on the initially precipitated powder.

(Ag(^mcytosine)₂)₄·[H₂V₁₀O₂₈]·14H₂O (Ag₄-V₁₀). A stock solution of the POM was prepared by dissolving V₁₀ (0.18 mol, 250 mg) in H₂O (10 mL). The V₁₀ solution (1.42 mL, 50 μmol) was added to a solution of freshly prepared AgC₂ to give a 4:1 AgC₂:V₁₀ ratio. Immediately, a light-orange suspension formed. Again, addition of H₂O (16.4 mL) did not redissolve the orange suspension. The solution was centrifuged, and the collected powder was dried in a

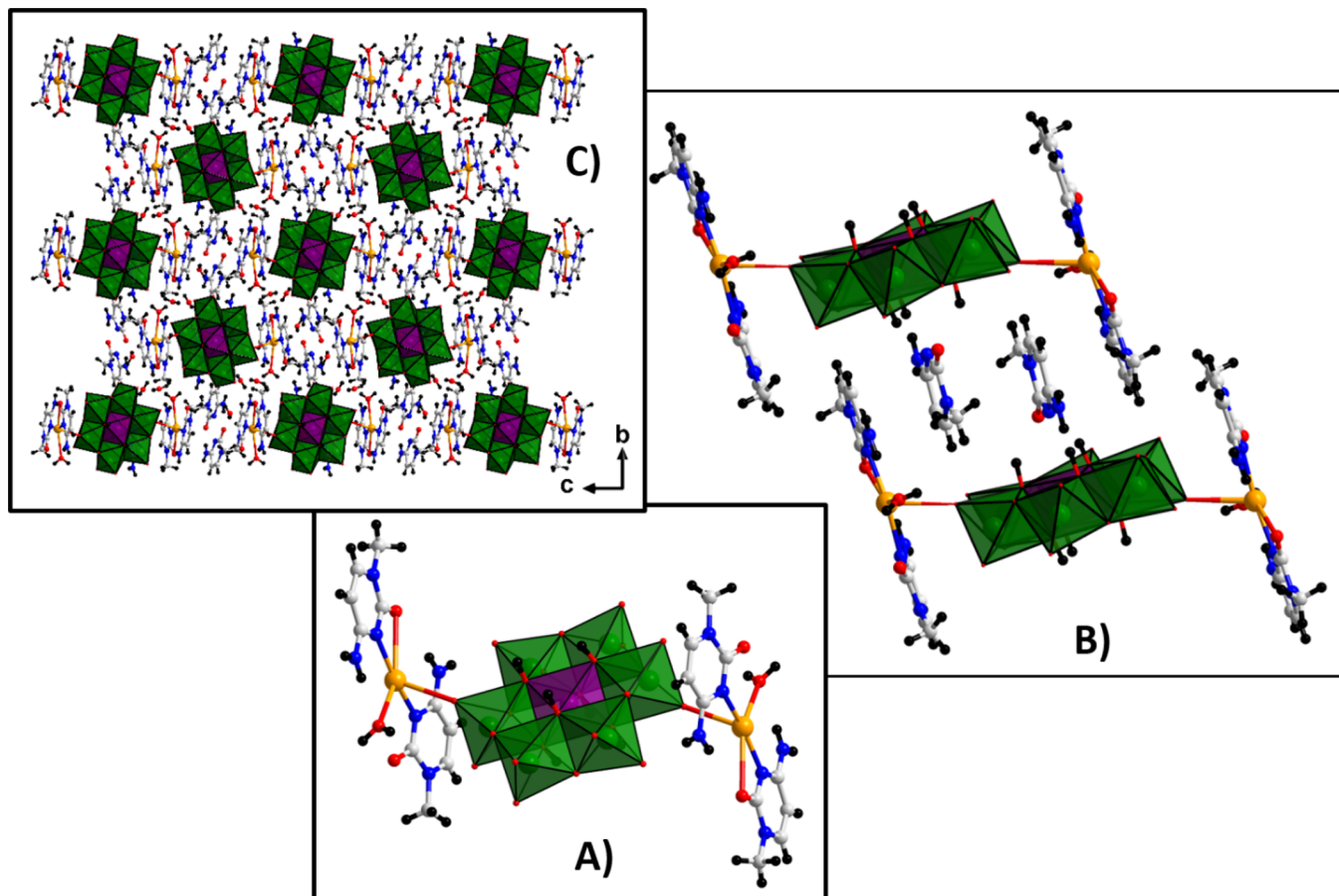


Figure 2. Views of $\text{Ag}_2\text{-CrMo}_6$. (A) Single CrMo_6 -POM capped by two $[\text{Ag}^{(\text{m}-\text{cytosine})_2}]^+$ complexes. (B) Two POM–Ag– $^{\text{m}}$ cytosine units plus two free cytosine molecules, highlighting the $\pi-\pi$ stacking between the free molecules and those coordinating silver, driving assembly of the crystallized lattice. (C) View down the a -axis showing eclipsed stacking of the POMs. Color code: green polyhedra are Mo, purple polyhedra are Cr, orange spheres are Ag, gray spheres are C, red spheres are O, and black spheres are H.

vacuum oven overnight for further characterization. The supernatant, left in the dark overnight, yielded light-orange, needle-like single crystals suitable for X-ray diffraction. Again, bulk characterization was performed on the powders, given the small quantity of crystals obtained.

($\text{Ag}_3(\text{m}-\text{cytosine})_5)_2[\text{Nb}_{10}\text{O}_{28}] \cdot 8\text{H}_2\text{O}$ ($\text{Ag}_6\text{-Nb}_{10}$). A stock solution of the POM was prepared by dissolving Nb_{10} (0.137 mmol, 250 mg) in water (10 mL). We added Nb_{10} solution (2.3 mL, 25 μmol) to a solution of freshly prepared AgC_2 . Immediately, a white suspension formed. Like the prior two reactions, addition of more water did not redissolve this very insoluble hybrid material. The precipitate was collected by centrifugation and dried in a vacuum oven overnight. Unlike the prior described reactions, crystals never formed from the supernatant. To obtain single crystals suitable for structural analysis, the precipitate was dissolved in an acetonitrile: H_2O (4:1) mixture. After 1 month, small single crystals had formed in the solution that were suitable for X-ray diffraction and comparison to bulk analysis of the powder.

Single-Crystal X-ray Diffraction. Single-crystal X-ray diffraction (SCXRD) for all structures were collected at 103 K, on a Rigaku Oxford Diffraction Synergy-S equipped with a PhotonJet-S Cu source ($\lambda = 1.54178 \text{ \AA}$) and a HyPix-6000HE photon counting detector. All the images were collected and processed using CrysAlisPro Versions 40.21a, 40.53, and 40.81a (Rigaku Oxford Diffraction, 2018).⁵⁶ After integration, both numerical (Gaussian) absorption and empirical absorption (spherical harmonic, image scaling, and detector scaling) corrections were applied.⁵⁷ All structures were solved by the intrinsic phasing method from the SHELXT program,⁵⁸ developed by successive difference Fourier syntheses, and refined by full-matrix

least-squares on all F2 data using SHELX⁵⁹ via the OLEX2 interface.⁶⁰

The crystallographic data for each compound can be obtained, free of charge, from The Cambridge Crystallographic Data Centre (<https://www.ccdc.cam.ac.uk/structures/>) citing CCDC numbers 2102482–2102485 and 2103588. Crystallographic information for the five structures is summarized in Tables 1 and 2.

Fourier Transform Infrared Spectroscopy (FT-IR). Spectra were recorded on a Nicolet iS10 FT-IR spectrometer with a secondary Nicolet iZ 10 module purchased from Thermo Fisher Scientific, Inc. The instrument was equipped with a diamond plate for attenuated total reflectance (ATR) measurements. Spectra were recorded in air.

Powder X-ray Diffraction (PXRD). The PXRD data of precipitated powders were collected on a Rigaku Miniflex diffractometer 600 (Cu $\text{K}\alpha$ irradiation, $\lambda = 1.54 \text{ \AA}$) in the range from 2 to 50° (2θ) with a scan speed of 1.0°/min and a step size of 0.02°.

RESULTS AND DISCUSSION

Synthesis and Product Yields. All these scoping experiments were done on a very small scale due to the expense of the $^{\text{m}}$ cytosine. The rapidly precipitated powders were in small amounts, estimated to be $\sim 10 \text{ mg}$. The reported Ag:POM ratios of the V_{10} and CrMo_6 reactions were those that yielded single crystals, after the majority of the $\text{Ag}-\text{m}-\text{cytosine}-\text{POM}$ complex had precipitated. This was also attempted with Nb_{10} , but since single crystals never grew from water, we now assume that the best ratio would be 6:1 Ag:Nb_{10} for a bulk product,

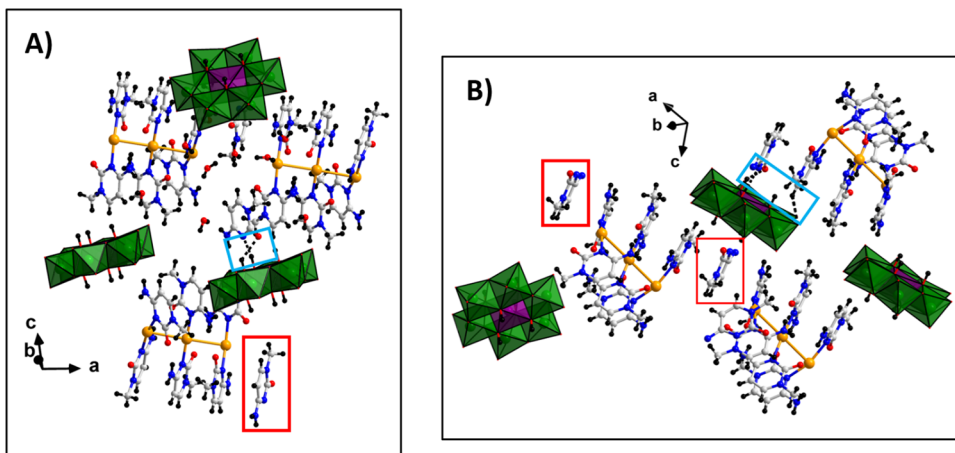


Figure 3. Views of the molecular components of $\text{Ag}_3\text{-CrMo}_6\text{-1}$ (A) and $\text{Ag}_3\text{-CrMo}_6\text{-2}$ (B). The color code is the same as described in Figure 1. Highlighted in the red boxes are the free ${}^m\text{cytosine}$ molecules that undergo $\pi-\pi$ stacking with the Ag-bound ${}^m\text{cytosine}$. The turquoise boxes highlight H-bonding interactions between the POM and free and bound ${}^m\text{cytosine}$. The atom color code is the same as Figure 2.

but this was never investigated. Because both the CrMo_6 and Nb_{10} Ag:POM synthesis ratios are $\sim 50\%$ Ag-deficient compared to the precipitated and crystallized product, we presume a maximum yield of $\sim 60\text{--}65\%$ for both of these. The V_{10} experiment was optimized at a 4:1 Ag:POM ratio, so a higher yield, closer to 90%, is estimated.

We assume that a yield close to 100% for bulk powders is possible with the correct Ag:POM ratio because the solids that rapidly precipitate are extremely insoluble in water. In the same vein, the very rapid precipitation of the observed phases suggests that it is probably difficult to obtain different Ag:POM ratios in crystallized lattices by employing different Ag:POM ratios in the reaction solutions.

Structures with $[\text{CrMo}_6(\text{OH})_6\text{O}_{18}]^{3-}$. Three different unit cells were identified among the crystals that grew out of the supernatant from the reaction between CrMo_6 and AgC_2 . The crystals all appeared very light pink in color, indicating the presence of the Cr-centered POM. The three different structures, all described below, will be referred to as $\text{Ag}_2\text{-CrMo}_6$, $\text{Ag}_3\text{-CrMo}_6\text{-1}$, and $\text{Ag}_3\text{-CrMo}_6\text{-2}$. Briefly, the $[\text{CrMo}_6(\text{OH})_6\text{O}_{18}]^{3-}$ POM (Figure 2A) contains a central octahedral Cr^{3+} with all $\text{Cr}-\text{O}$ bonds $\sim 1.95\text{--}1.98 \text{ \AA}$ for all three reported structures. Bond valence sum (BVS, Tables S1–S3) calculations indicate that the oxidation state did not change in the synthesis. The Cr octahedron shares edges with six distorted MoO_6 octahedra, which all share edges with each other in a ring, creating a flat, compact hexagonal-shaped cluster. Each Mo^{VI} has two terminal yl -oxo bonds ($\text{Mo}=\text{O}_{\text{yl}}$ of $\sim 1.7 \text{ \AA}$), two $\mu_2\text{-O-Mo}$ bonds (Mo-O of $\sim 1.90\text{--}1.98 \text{ \AA}$), and two $\mu_3\text{-OH-Mo}$ trans to the two $\text{Mo}=\text{O}_{\text{yl}}$ moieties (Mo-OH of $\sim 2.3 \text{ \AA}$). For all three structures, there are six $\mu_3\text{-OH}$ moieties per POM, three on each face of the hexagonally shaped cluster (confirmed by bond valence sum calculations, Tables S1–S3). The $[\text{Ag}(\text{N}3\text{-}{}^m\text{cytosine})_2]^{+}$ complexes are also similar for each structure (and also with V_{10}), and the ${}^m\text{cytosine}$ ligands bind to a central Ag^+ , in a nearly linear arrangement, featuring an N3 binding mode with a Ag-N bond distance of $2.1\text{--}2.2 \text{ \AA}$.^{13–16,32}

$\text{Ag}_2\text{-CrMo}_6$: $\text{Ag}_2\text{-CrMo}_6$ crystallizes in the monoclinic space group $P2_1/c$ (no. 14) with a unit cell volume of $3677.82(5) \text{ \AA}^3$ and is fully formulated as $(\text{Ag}(\text{C}_5\text{H}_7\text{ON}_3)_2)_2 \cdot [\text{C}_5\text{H}_{7.5}\text{ON}_3]_2[\text{CrMo}_6(\text{OH})_6\text{O}_{18}] \cdot 17\text{H}_2\text{O}$. This is the only CrMo_6 complex that does not feature argentophilic inter-

actions between the $[\text{Ag}(\text{N}3\text{-}{}^m\text{cytosine})_2]^{+}$ base pairs. Rather, each POM bonds to two crystallographically equivalent $[\text{Ag}(\text{N}3\text{-}{}^m\text{cytosine})_2]^{+}$ units via $\text{Mo}=\text{O}_{\text{yl}}\text{-Ag}$ with an $\text{O}_{\text{yl}}\text{-Ag}$ bond distance of $2.673(3) \text{ \AA}$ (Figure 2A). The bond length is consistent with prior reported Ag-O_{yl} bond lengths reported for other Anderson Ag systems.^{27–29} In the $[\text{Ag}(\text{N}3\text{-}{}^m\text{cytosine})_2]^{+}$ base pairs, the Ag^+ binds to the N3 atom of each ${}^m\text{cytosine}$ base ($\langle \text{N}3\text{-Ag-N}3 \rangle = 161.94^\circ$), which is in a transoid orientation (anti-Watson-Crick) as previously observed for silver-cytosine base pairs in a DNA structure.⁶¹ The ${}^m\text{cytosine}$ bases are in a nearly coplanar arrangement (interplanar angles of ca. 10°) enabling the formation of hydrogen bonds between keto and amino groups of opposite ${}^m\text{cytosine}$ bases ($\text{NH}\cdots\text{O} = 2.479 \text{ \AA}$). The coordination geometry of Ag^+ is approximately “seesaw-shaped”, completed by the bond to $\text{Mo}=\text{O}_{\text{yl}}\text{-Ag}$ and a water molecule ($\text{Ag-O}_{\text{water}} = 2.9 \text{ \AA}$) with an $\text{O}_{\text{yl}}\text{-Ag-O}_{\text{w}}$ bond angle of 72° .

There are two free ${}^m\text{cytosine}$ ligands per cluster, and we presume that half of them are protonated at the N3 position to complete the charge balance, and this is described as $[(\text{H}_{0.5})\text{C}_5\text{H}_7\text{ON}_3]$. BVS of the ${}^m\text{cytosine}$ nitrogens of the unbound molecule (Table S1, N8) showed the N3 position to be lower than the other two (2.5 vs 3.3/3/4), consistent with partial protonation of this site. The presence of free ${}^m\text{cytosine}$ (not bound to Ag) in the structures suggests that these ligands are labile in solution and as demonstrated here can lead to higher complexity and diversity of crystallized lattices. This is further reinforced later in the $\text{Ag}_6\text{-Nb}_{10}$ structure, which contains a cytosine-“deficient” $\text{Ag}_3({}^m\text{cytosine})_5$ cluster.

The arrangement of the free ${}^m\text{cytosine}$ ligand and the ${}^m\text{cytosine-Ag-POM}$ complex is clearly dictated by interactions between these lattice components. Figure 2B highlights the $\pi-\pi$ stacking between the free and bound ${}^m\text{cytosine}$, with $\sim 3 \text{ \AA}$ between the rings (the shortest distance of 2.7 \AA measured between the nitrogen atom of the amino group of one ring and the methyl proton of the neighboring ring). There is also H-bonding between the POM OH ligands and the free ${}^m\text{cytosine}$ molecules. For example, the carbonyl O---HO-POM distance is 1.99 \AA , while the N3---HO-POM distance is 1.76 \AA . There is also H-bonding of the lattice water molecules, particularly to the carbonyl oxygens of the ${}^m\text{cytosine}$ molecules and to the POMs. The CrMo_6 units are aligned in an eclipsed fashion along the a -axis, observed in

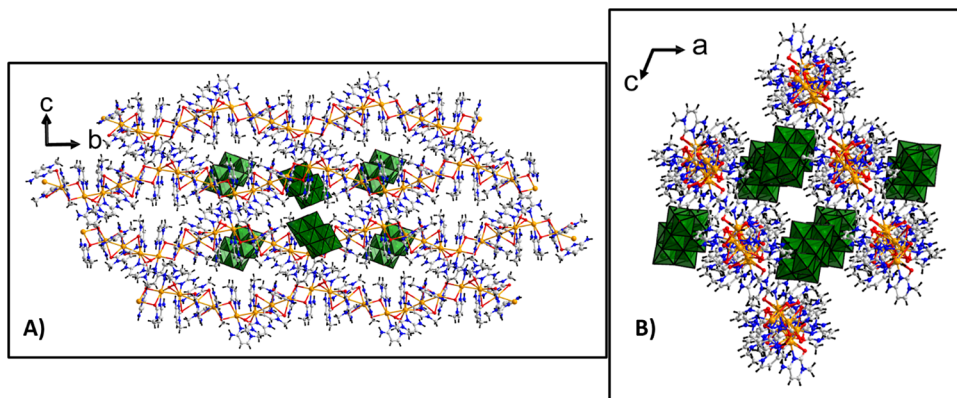


Figure 4. Unit cell views of $\text{Ag}_4\cdot\text{V}_{10}$ down the a -axis (A) and b -axis (B). Green polyhedra are V_{10} POMs, orange spheres are Ag, blue spheres are N, gray spheres are C, black spheres are H, red spheres are O.

Figure 2C. This structure demonstrates that m cytosine–Ag–POM direct bonding via Ag–O_{POM} is achievable (as with the Nb₁₀ POM, discussed later) as a potential step toward building Ag–base pairs and Ag–DNA scaffolds with POM linkers. The strongest driving force of crystallization of this particular structure appears to be π – π stacking of the free and coordinated m cytosine molecules, also important in assembling the metallo-DNA complexes.

$\text{Ag}_3\text{-CrMo}_6\text{-1}$ and $\text{Ag}_3\text{-CrMo}_6\text{-2}$. The other two compounds obtained are given the descriptive names $\text{Ag}_3\text{-CrMo}_6\text{-1}$ and $\text{Ag}_3\text{-CrMo}_6\text{-2}$. Full formulae are $(\text{Ag}(\text{C}_5\text{H}_7\text{ON}_3)_2)_3\cdot[\text{CrMo}_6(\text{OH})_6\text{O}_{18}]\cdot17\text{H}_2\text{O}, 2(\text{C}_5\text{H}_7\text{ON}_3)$ and $(\text{Ag}(\text{C}_5\text{H}_7\text{ON}_3)_2)_3\cdot[\text{CrMo}_6(\text{OH})_6\text{O}_{18}]\cdot14\text{H}_2\text{O}, 2(\text{C}_5\text{H}_7\text{ON}_3)$, respectively. These two structures will be discussed together, given their similarities. The only difference in their formulae is the number of lattice water molecules. Both structures crystallize in the monoclinic $C2/c$ (no. 15) space group but with slightly different cell volumes due to the number of lattice waters. $\text{Ag}_3\text{-CrMo}_6\text{-1}$ has a cell volume of $8428.37(13)\text{ \AA}^3$, and $\text{Ag}_3\text{-CrMo}_6\text{-2}$ has a cell volume of $8092.4(9)\text{ \AA}^3$. Both $\text{Ag}_3\text{-CrMo}_6\text{-1}$ and $\text{Ag}_3\text{-CrMo}_6\text{-2}$, like $\text{Ag}_2\text{-CrMo}_6$, contain a hexaprotonated $[\text{CrMo}_6(\text{OH})_6\text{O}_{18}]^{3-}$ POM that is charge-balanced by three Ag⁺ cations within a $[\text{Ag}({}^m\text{cytosine})_2]_3$ helix. These structures resemble those previously published for $[\text{Ag}({}^m\text{cytosine})]^+$ complex derivatives^{13,15,16} but differ in that, for the first time, an uninterrupted chain is not formed. Rather, the chain length seems to be determined by the anionic charge of the POM. These structures constitute the first example of cytosine–Ag–cytosine trimers and establish a methodology for studying these types of shorter structures whose length can be dictated by the anionic charge of the POM (as with $\text{Ag}_4\cdot\text{V}_{10}$, discussed later). This is of great importance in the field of metallo-DNA systems.⁶² The Ag⁺ are not bonded to the POM, but rather, they form a trimer with a linear Ag–Ag–Ag chain with Ag–Ag distances of $\sim 3.19\text{ \AA}$ for $\text{Ag}_3\text{-CrMo}_6\text{-1}$ and 3.21 \AA for $\text{Ag}_3\text{-CrMo}_6\text{-2}$, illustrated in Figure 3A,B. They are fairly typical argentophilic interactions.⁴ The Ag–Ag–Ag axis is very close to linear for each (176.9 and 178.7° , respectively). While in the $\text{Ag}_3\text{-CrMo}_6\text{-1}$, the m cytosine bases adopt a slight cisoid conformation and are twisted from coplanarity, they are in a more perpendicular orientation in the $\text{Ag}_3\text{-CrMo}_6\text{-2}$ (interplanar angles of 77.26 – 79.40°). In addition, the N–Ag–N axis of each is offset from the neighboring N–Ag–N, similar to the helical twist of DNA (Figure S4). These structures are supported by intramolecular

hydrogen bonds formed between the pyrimidine rings of contiguous $[\text{Ag}({}^m\text{cytosine})_2]^+$ pairs.

Analogous to the above described $\text{Ag}_2\text{-CrMo}_6$, both Ag_3 lattices contain two free m cytosine per cluster, which are associated by π – π stacking with those bonded to Ag⁺ (highlighted in red boxes in Figure 3A,B). For $\text{Ag}_3\text{-CrMo}_6\text{-2}$ (Figure 3B), the free m cytosine molecules alternate with the bonded m cytosine approximately along the (110) axis, with ring distances of around 3.4 \AA . Also, like $\text{Ag}_2\text{-CrMo}_6$, there is H-bonding between the POM and the m cytosine. They are highlighted in the turquoise boxes in Figure 3 and shown in detail in Figure S5. There are three primary hydrogen bonds between the POM and the bound m cytosine in each structure. For $\text{Ag}_3\text{-CrMo}_6\text{-1}$, the free m cytosine is hydrogen-bonded at the endocyclic N3 atom (H-bonding length of 1.8 \AA) and the carbonyl group (H-bonding of 1.7 \AA) with protons on the face of the POM. The stronger H bond to the m cytosine–N3 atom may be one explanation of the free m cytosine in the structure, even though it is not required for charge balance. There is also H-bonding between the methyl-bound nitrogen to O_y=Mo of the POM. The H bonds for $\text{Ag}_3\text{-CrMo}_6\text{-2}$ involve the equivalent atoms but with shorter bonds (1.7 and 1.8 \AA , highlighted in Figure S5).

Finally, the unit cell views down the b -axis for $\text{Ag}_3\text{-CrMo}_6\text{-1}$ and $\text{Ag}_3\text{-CrMo}_6\text{-2}$ are compared in Figure S6, and the similarities and small differences are evident. Both feature alternating layers of CrMo₆ along the a -axis (and the b -axis), and the layers are stacked in the c -direction. Differences include the following: (1) the flat CrMo₆ clusters are more tilted out of the ab -plane in $\text{Ag}_3\text{-CrMo}_6\text{-2}$, compared to $\text{Ag}_3\text{-CrMo}_6\text{-1}$; (2) the Ag₃ units are aligned approximately parallel to the a -axis for $\text{Ag}_3\text{-CrMo}_6\text{-2}$ and are slightly angled off the a -direction for $\text{Ag}_3\text{-CrMo}_6\text{-1}$. In summary, the two cocrystallized lattices that phase segregate rather than form a single disordered phase reflect the many strong yet flexible noncovalent interactions between the molecular components, which include π – π stacking, hydrogen-bonding, and argento-philic interactions.

As previously mentioned, one hypothesis formulated from the dominance of the $\text{Ag}_3\text{-CrMo}_6$ assemblies in the obtained single crystals is that the charge on the POM can be used to control the Ag chain length, and crystallization of $\text{Ag}_4\cdot\text{V}_{10}$ strengthened this argument. $\text{Ag}_4\cdot\text{V}_{10}$ crystallizes in the monoclinic space group $P2_1/n$ with a cell volume of $8713.6(2)\text{ \AA}^3$, formulated as $(\text{Ag}(\text{C}_5\text{H}_7\text{ON}_3)_2)_4\cdot[\text{H}_2\text{V}_{10}\text{O}_{28}]\cdot14\text{H}_2\text{O}$. The silver chains are the length of the negative charge on the

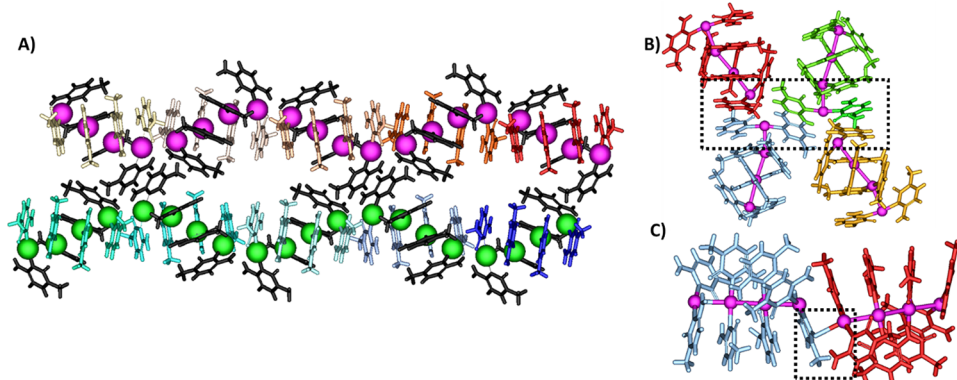


Figure 5. Highlighting the Ag tetramers and chains (pseudo-helices) within the $\text{Ag}_4\text{-V}_{10}$ lattice. Each Ag_4 -cytosine unit is represented by a distinctive color, and Ag is shown as pink and green spheres for ease of viewing. (A) Two partial chains running along the b -axis. (B) Expanded view of the $\pi-\pi$ stacking between Ag chains and Ag chains. (C) Expanded view of the $\text{Ag}-\text{O}_{\text{mcyt}}$ bond between $\text{Ag}_4\text{-V}_{10}$ lattices.

POM ($4-$, Ag_4 chain), comprising four $[\text{Ag}(\text{N3-}^{\text{m}}\text{cytosine})_2]$ pairs, and not connected to the POM, analogous to the $\text{Ag}_3\text{-CrMo}_6$ lattices. However, here, the Ag_4 chains can be considered joined into infinite pseudo-helices, highlighted in Figures 4A and 5. The Ag–Ag distances within the Ag_4 unit are $\sim 3.1 \text{ \AA}$, with 4.0 \AA between Ag_4 units, which is not considered a Ag–Ag interaction. Instead, $\text{Ag}_4\text{-V}_{10}$ double helices are linked by a coordination bond between the Ag^+ of a terminal $[\text{Ag}(\text{N3-}^{\text{m}}\text{cytosine})_2]$ pair and the carbonyl group of the initial pair of the next helix, with $\text{Ag}-\text{O}_{\text{mcyt}}$ bond distances ranging from 2.7 to 2.9 \AA , highlighted in Figure 5C. The pseudo-helices arise from the Ag–Ag–Ag angles within and between tetramers. Within the linear tetramer, these angles are in the range of 159.21 – 175.99° and between the tetramers are 147.23 – 149.40° . Like in the $\text{Ag}_3\text{-CrMo}_6$ lattices, the ${}^{\text{m}}$ cytosine bases adopt a cisoid conformation and are twisted from coplanarity (interplanar angles of 67.89 – 79.08°). The pseudo-helices are aligned along the b -axis (Figures 4 and 5A). In addition, $\pi-\pi$ stacking of ${}^{\text{m}}$ cytosine is observed along and between individual Ag_4 chains (Figure 5B). It should be noted that the 1D linear structure formed by $[\text{Ag}(\text{N3-}^{\text{m}}\text{cytosine})_2]^+$ base pairs differs from those described in the literature^{13,15,16} in that there are four types of interactions that keep the 1D structure uninterrupted: Ag–Ag, $\text{Ag}-\text{O}_{\text{mcyt}}$ intramolecular hydrogen bonds, and $\pi-\pi$ interactions. Moreover, $\pi-\pi$ stacking interactions also exist between neighboring chains and occur every two Ag_4 units, and these interactions define a 2D array within the bc -plane, illustrated in Figure 5A. A view down the b -axis (Figure 5B) highlights the location of the decavanadate POMs between the chains, also approximately aligned along the b -axis. Interestingly, interactions between the V_{10} units and the Ag chains are almost negligible.

Briefly, $[\text{H}_2\text{V}_{10}\text{O}_{28}]^{4-}$ is typical for prior reported structures, except for lack of V_{10} – V_{10} dimerization via H-bonding. It can be described as a 2×3 rectangle of mutually edge-sharing VO_6 octahedra. The two central octahedra along the long edge do not have an yl -oxo, and the rectangle is capped on each face with two additional VO_6 octahedra. Doubly protonated decavanadate with a $4-$ charge is very commonly observed, first noted by Klempar et al. in 1987.³⁹ This common protonation pattern drives V_{10} – V_{10} association in the solid state and solution.^{40,43} We could not directly locate the two protons on V_{10} in the $\text{Ag}_4\text{-V}_{10}$ lattice, but rather, their existence is implied by charge balance requirements and knowledge of the common protonation of decavanadate. BVS calculations

(Table S4 and Figure S7) describe the most likely sites for protonation as side-by-side $\mu_2\text{-O}$ and $\mu_3\text{-O}$, consistent with prior reported V_{10} .⁶³ Because these protonated sites do not play a role in supramolecular assembly, we suggest that the argentophilic and $\pi-\pi$ stacking interactions of the $\text{Ag}-{}^{\text{m}}$ cytosine complexes are the strongest noncovalent bonding associations and driving forces in lattice formation. In addition, this structure taken together with the $\text{Ag}_3\text{-CrMo}_6$ structures implies that the POM charge can influence the Ag chain length. Interestingly, the prior reported Ag-DMSO-V_{10} composite phase²⁷ presents a different viewpoint, where Ag_3 chains link the V_{10} clusters in one direction and Ag_1 links them in a perpendicular direction in a two-dimensional network.

For both the V_{10} POM and the CrMo_6 POM, $\pi-\pi$ stacking and argentophilic associations appear to drive assembly processes and lattice organization, while the POM may influence the Ag chain length formed by Ag–Ag interactions. In a fifth lattice exploiting the $[\text{Nb}_{10}\text{O}_{28}]^{6-}$ (decaniobate, Nb_{10}) POM, we observe strong Ag–POM interactions in addition to the Ag–Ag associations and $\pi-\pi$ stacking of the ${}^{\text{m}}$ cytosine ligands. Nb_{10} is isostructural with V_{10} , but unlike V_{10} , it is generally not protonated in solid-state structures. $\text{Ag}_6\text{-Nb}_{10}$ (Figure 6) crystallizes in the triclinic $\text{P}1$ unit cell ($2304.4(14) \text{ \AA}^3$), with a moiety formula of

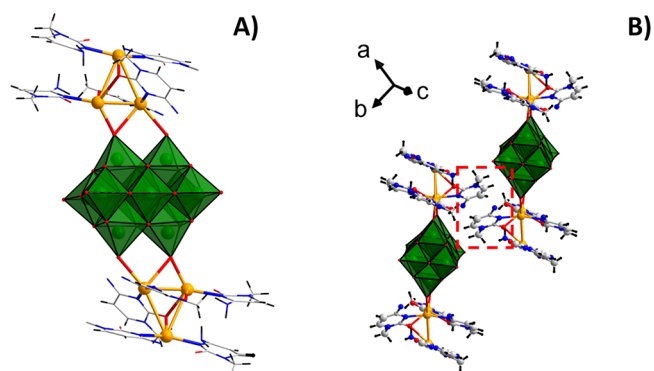


Figure 6. (A) View of the $(\text{Ag}_3(\text{C}_5\text{H}_7\text{ON}_3)_5)_2[\text{Nb}_{10}\text{O}_{28}]$ composite molecule of $\text{Ag}_6\text{-Nb}_{10}$, highlighting the Ag–Ag and Ag–POM bonding. (B) Two adjacent molecules, highlighting intermolecular $\pi-\pi$ stacking (in the dashed red box). Green polyhedra are Nb polyhedra of the POM, yellow spheres are Ag, blue is N, red is carbon, and black is hydrogen.

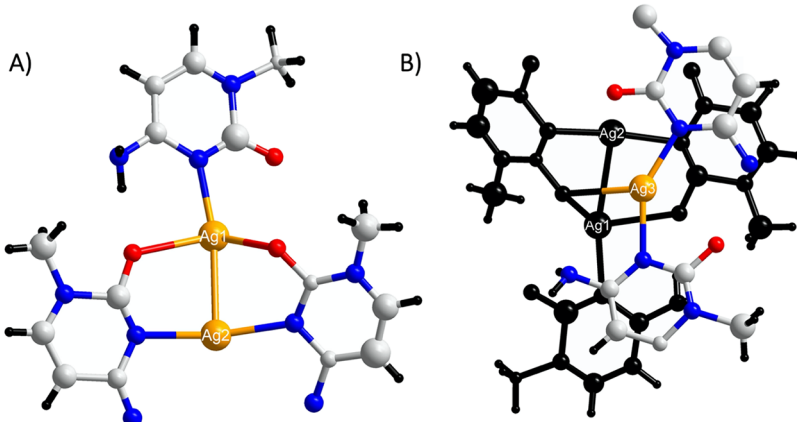


Figure 7. (A) Simplified view of the bimetallic $[Ag_2(N3,O2\text{-}^m\text{cytosine})_2]^{2+}$ fragment with a third ${}^m\text{cytosine}$ bound through the $Ag1\text{-}N_{m\text{cyt}}$ bond. (B) View of the $[Ag(N3\text{-}{}^m\text{cytosine})_2]^+$ formed above the bimetallic base pair and linked via the $Ag3\text{-}O_{2\text{cyt}'}$ bond (in this case, the bimetallic base pair is displayed in black for clarity).

$(Ag_3(C_5H_7ON_3)_5)_2[Nb_{10}O_{28}] \cdot 8H_2O$. On the “top” and “bottom” of the Nb_{10} cluster, there are two Ag^+ ions bonded (four total) to the four most basic^{21,64} $Nb=O_t$ oxygens. $Ag1$ is bonded once with a $Nb=O_t\text{-}Ag$ bond length of 2.35 Å, and $Ag2$ bridges the two juxtaposed yl-oxos with $Nb=O_t\text{-}Ag$ bond lengths of 2.66 and 2.71 Å. While $Ag2$ has $Ag\text{-}O$ bond lengths similar to those of the $Ag_2\text{-CrMo}_6$ structure, the single $Nb=O_t\text{-}Ag1$ bond is quite short. $Ag1\text{-}Ag2$ also has a short interaction distance of ~2.9 Å. A third silver cation ($Ag3$) is respectively 3.4 and 3.5 Å from $Ag2$ and $Ag1$. The analogous Ag^+_3 -triangular aggregate is well-known but much scarcer in Ag chemistry.⁴ A silver trimer in simple aqueous silver nitrate was detected by mass spectrometry and predicted to be the molecular precursor to Ag triangularly shaped nanostructures.⁶⁵ In addition, an Ag^+_3 , oxo-capped with a benzoquinone ligand, has been structurally characterized,⁶⁶ and these silver trimers are of interest for their luminescent properties. For the prior reported Ag^+_3 triangles (two structures), both have two $Ag\text{-}Ag$ distances of ~3.4 Å and one of ~3.7 Å. Comparing the average of the three $Ag\text{-}Ag$ bonds of the three structures, the prior reported, quinone-capped Ag^+_3 has a $[Ag\text{-}Ag]_{avg}$ of 3.5 Å, and the Ag^+_3 triangle described here in $Ag_6\text{-Nb}_{10}$ has a $[Ag\text{-}Ag]_{avg}$ of 3.3 Å. While a ${}^m\text{cytosine}$ ligand bridges the $Ag\text{-}Ag = 3.5$ Å triangle edge ($Ag\text{-}O_{cyt}$ of ~2.6 Å), it is arguably not bonded to the third silver because the $Ag\text{-}O$ distance is very long, approximately 3.1 Å.

Another unique aspect of the $Ag\text{-}{}^m\text{cytosine}$ cluster of $Ag_6\text{-Nb}_{10}$ is $Ag1$. It has the shortest $Nb=O_y\text{-}Ag$ bond and the shortest $Ag\text{-}Ag$ interaction, and it is bound to only one ${}^m\text{cytosine}$ ligand. Like the four additional structures reported here, $Ag_6\text{-Nb}_{10}$ exhibits $\pi\text{-}\pi$ stacking between the neighboring $Ag_6\text{-Nb}_{10}$ -units, highlighted in Figure 6B.

Importantly, a unique arrangement is observed for these silver- ${}^m\text{cytosine}$ pairs. $Ag1$ and $Ag2$ ions participate in the formation of the base pair $[Ag_2(N3,O2\text{-}{}^m\text{cytosine})_2]^{2+}$ by joining two different ${}^m\text{cytosines}$ (${}^m\text{cyt}$ and ${}^m\text{cyt}'$) in the coordination modes $N3_{m\text{cyt}}\text{-}Ag2\text{-}N3_{m\text{cyt}'}$ ($N\text{-}Ag$ of 2.222 and 2.255 Å) and $O2_{m\text{cyt}}\text{-}Ag1\text{-}O2_{m\text{cyt}'}$ ($O\text{-}Ag$ of 2.585 and 2.554 Å), therefore adopting a cisoid conformation (Figure 7A). In addition, a third ${}^m\text{cytosine}$ (${}^m\text{cyt}''$) binds to this bimetallic base pair through $Ag1$, forming a $Ag1\text{-}N3_{m\text{cyt}''}$ coordination bond ($N\text{-}Ag$ of 2.219 Å) and a hydrogen bond through ${}^m\text{cyt}''\text{-NH}_2$ and ${}^m\text{cyt}'\text{-keto}$ groups. To the best of our knowledge, this is the first described example of a bimetallic silver-cytosine pair

showing these coordination modes between complementary cytosine. Above this new silver-cytosine system, the $[Ag\text{-}({}^m\text{cytosine})_2]^+$ base pair is also formed with a transoid conformation and bound to the previous bimetallic base pair via the $Ag3\text{-}O_{cyt}''$ ($O\text{-}Ag$ of 2.646 Å) coordination bond (Figure 7B). These results are of special interest in the field of silver-DNA systems, including the generation of silver nanoclusters using polycytosine sequences, since they provide structural evidence for the formation of new silver-cytosine pairs that bind two silver ions in a Watson-Crick orientation, leading to $Ag\text{-}Ag$ interactions within the same base pair. In addition, this arrangement shows to be adequate to bind an adjacent silver-cytosine pair via a $Ag\text{-}O$ coordination bond.

Characterization of Bulk Precipitates. All reaction solutions precipitated rapidly upon combining the aqueous solutions of the POM and the *in situ* formed silver- ${}^m\text{cytosine}$ complex due to the poor solubility of the hybrid phases. These precipitates represent the majority of the dissolved starting materials, while subsequent formation of crystals represents a minor component, compared to the bulk. Attempts to recrystallize the $CrMo_6$ and V_{10} precipitates in acetonitrile-water mixtures were unsuccessful. The $Ag\text{-}{}^m\text{cytosine-CrMo}_6$ powders were not soluble in acetonitrile-water mixtures. The $Ag\text{-}{}^m\text{cytosine-V}_{10}$ powders dissolved in acetonitrile-water but never yielded crystals, even after several months. It is particularly important to determine if the rapidly precipitated bulk is a microcrystalline form of the single crystals that were analyzed. Infrared spectroscopy and powder X-ray diffraction (PXRD) of both the precipitates and the single-crystal forms yielded some information. The analyses of the crystals deposited from the $Ag\text{-}{}^m\text{cytosine-CrMo}_6$ reaction were carried out on the mixture of three crystal types. Their separation was not feasible due to the small volume, similarity in color, and similarity in the morphologies of $Ag_3\text{-CrMo}_6\text{-1}$ and $Ag_3\text{-CrMo}_6\text{-2}$ (Figure S8). Infrared spectra of the precipitates obtained from combining the $Ag\text{-}{}^m\text{cytosine}$ solution with the three POM solutions are shown in Figures S1, S2, and S3, respectively, for $POM = CrMo_6, V_{10},$ and Nb_{10} . For $CrMo_6$ and V_{10} , we also show the IR spectra for the crystals but not for Nb_{10} due to scarcity of samples. Also shown in Figures S1–S3 are the IR spectra for the parent sodium salts of $CrMo_6$ and V_{10} and the tetramethylammonium (TMA) salt of Nb_{10} , referred to prior. Importantly, for all three precipitates, bands for both the POM and the $Ag\text{-}{}^m\text{cytosine}$ complex are

observed, indicating that we are not simply precipitating the starting material. For all three POMs, the metal–oxygen vibrations are more distinct in the hybrid materials with Ag–^mcytosine, compared to the POM starting materials. This is due to minimal H-bonding with water, which is so prevalent in the lattices of the starting materials. For Nb₁₀, we are able to follow the fate of the counterion (TMA) since it has signature vibrational bands in the IR spectrum. We observe that there is no TMA in the Ag–^mcytosine–Nb₁₀ precipitate, indicating that there is complete ion exchange of Ag⁺–^mcytosine complexes for TMA⁺. For CrMo₆ and V₁₀, the IR spectra of the precipitates and crystals appear similar, indicating that similar molecular units are present in both solids.

While IR is useful for identifying molecules in the Ag–^mcytosine–POM precipitates and crystals, it does not provide information on the arrangement of the molecules and the interactions that drive these arrangements. PXRD patterns of the precipitate from the Ag–^mcytosine–CrMo₆ reaction and the mixture of crystals deposited from the supernatant and simulated diffraction patterns from all three single-crystal structures of the Ag–^mcytosine–CrMo₆ system are shown in Figure S9. The simulated X-ray diffraction patterns of Ag₃-CrMo₆-1 and Ag₃-CrMo₆-2, as expected, are very similar. The (111) dominant peak at ~8.9° in both phases is also the dominant peak in both the precipitated powder and the mixed crystals. It is more difficult to definitively ascertain which of these phases dominates either the initially precipitated powder or the subsequently deposited crystals, given their similarities. However, the starred peak of the crystal diffraction pattern is unique to Ag₃-CrMo₆-2, and no unique peaks of Ag₃-CrMo₆-1 are apparent in the PXRD patterns of the deposited crystals. On the other hand, the dominant peak of Ag₂-CrMo₆ is barely visible in the PXRD baselines of both the precipitated powder and the subsequently deposited crystals, indicating that it is a minor phase. Since Ag₂-CrMo₆ features POM–Ag bonding and the other two phases contain Ag₃ linear trimers instead, we suggest that the Ag–POM interaction is not strong with this POM, and its main role in the assembly of these lattices is charge-balancing the Ag–^mcytosine polynuclear molecule, and taken together with the other structures, we can say that the POM charge also dictates the nuclearity of the Ag–^mcytosine chain.

PXRD patterns of neither the precipitate nor the crystals of Ag₄-V₁₀ match the diffraction pattern simulated from the single-crystal structure (Figure S10). Poor signal-to-noise ratios in both diffraction spectra indicate poor crystallinity, which we often attribute to desolvation of crystalline lattices, i.e., the loss of lattice water molecules that promote the long-range order through space filling and noncovalent interactions such as hydrogen bonding. This is most likely the case for the difference in the PXRD patterns of Ag₄-V₁₀ crystals compared to the simulated diffraction pattern from single-crystal data. The diffraction data of the precipitated solid has one strong peak that has a similar position to the major peak envelope of Ag₄-V₁₀ simulated diffraction, around 2θ = 9°. This bulk characterization by PXRD is very different from the above described results for the Ag-CrMo₆ phases and the later described results for Ag₆-Nb₁₀, which suggests that the crystallized Ag₄-V₁₀ architecture is flexible and alters with small changes such as the lattice solvent, in a way that the other lattices do not. The major structural difference between Ag₄-V₁₀ and the other four reported structures is the infinite

Ag₄ chains. The Ag₄ units are bridged by the ^mcytosine carbonyl (highlighted in Figures 5 and 6), and this linkage is likely flexible and labile in response to the local environment, leading to the poor order observed by PXRD of both the precipitate and the crushed crystals (crushed for PXRD measurement).

On the other hand, the PXRD pattern of the precipitate of Ag–^mcytosine–Nb₁₀ solution unambiguously matches the diffraction pattern simulated from the single-crystal data of Ag₆-Nb₁₀ (Figure 8). This is particularly pertinent for this

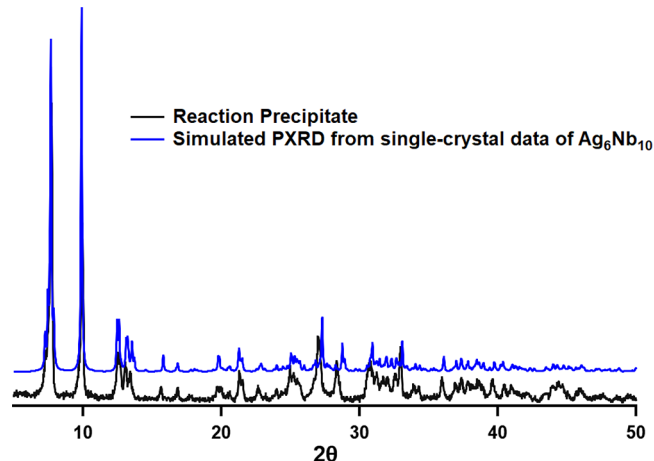


Figure 8. Comparing the PXRD patterns of the rapidly precipitated powder from the Ag–cytosine–Nb₁₀ (black) to the simulated diffraction spectra of Ag₆-Nb₁₀ (blue), which was obtained by dissolution of the precipitate and crystallization from an acetonitrile–water mixture.

phase because, unlike the V₁₀ and CrMo₆ POM studies, the crystals were not obtained from the same aqueous supernatant as the reaction precipitate. Rather, they were obtained from dissolution of the precipitated powder in an acetonitrile–water mixture (see the Experimental Methods). This is an important result, informing us that the assembly that we observe in Ag₆-Nb₁₀ is indeed the same as the bulk material precipitated from water rather than an arrangement promoted by the different solvent mixture (ACN/water) necessitated for redissolution. Moreover, since the bulk and the crystals were obtained from different solutions, this arrangement of lattice species is robust and contributes to our understanding of the potential multiple roles of POMs in engineering metal–DNA assemblies. In the future, we will consider additional solvent mixtures for crystallization as one strategy to either broaden the library of ^mcytosine–Ag–POM compounds or formulate rules to better predict their self-assembly.

CONCLUSIONS

The POM-[Ag(^mcytosine)₂]⁺ structures highlight and reinforce several important hypotheses and future strategies for exploiting POMs for designing and assembling Ag–DNA–POM and Ag–base–POM arrays. First, more basic POMs, such as polyoxoniobates, can be used to enforce Ag–POM bonding; i.e., necessary for capping and bridging Ag helix units as nodes and branching points in such putative materials. Second, in four examples (Ag₆-Nb₁₀, Ag₄-V₁₀, and the two Ag₃-CrMo₆ structures), we observe that the size of the Ag–cytosine polymer/cluster is correlated with the POM charge (directly related to its protonation state), meaning that the

charge can be used to help dictate Ag chain lengths in engineered complexes that mimic metal–DNA assemblies. To summarize, (1) the V₁₀ cluster has a 4– charge (doubly protonated) and crystallizes with a Ag₄ chain; (2) the CrMo₆ cluster has a 3– charge, and the major phases crystallized with the Ag₃ chain; (3) the Nb₁₀ cluster has a 6– charge, and it crystallizes with two associated Ag₃-triangular trimers bonded to each cluster. While the dominant arrangement of Ag⁺ ions appears to be linear, controlled by π – π stacking of the cytosines and argentophilic interactions, the unusual Ag⁺₃ triangle highlights another probable role in engineering supramolecular assembly of these multicomponent systems. Finally, intermolecular π – π stacking is one of the most prevalent noncovalent interactions observed in the assembly of the molecular components into crystalline lattices.

Future endeavors will be creating additional Ag–^mcytosine assemblies with polyoxoniobates and Nb-substituted POMs to confirm and exploit the hypothesis that more basic POMs are more effective in linking the Ag–cytosine molecules. We will also attempt to crystallize Ag–^mcytosine–POM complexes exploiting POMs of higher charge to further our understanding of the influence of the POM charge on Ag chain nuclearity. Ultimately, synthetic strategies and approaches will be applied to engineering metal–DNA–POM complexes in which the POM serves as a node and linker to metallo-DNA helices.

ASSOCIATED CONTENT

Supporting Information

The Supporting Information is available free of charge at <https://pubs.acs.org/doi/10.1021/acs.cgd.1c01385>.

Comparison of infrared (IR) spectra of single crystals and precipitated solids for the reported compounds, supplemental structure views of Ag₃–CrMo₆ compounds including highlighting of H-bonding, view of decavanadate locating protonated oxygens, microscope image (photo) of mixed Ag–cytosine–CrMo₆ crystals, PXRD comparing single-crystal samples and precipitated samples with X-ray patterns calculated from the single-crystal data, and tables of select bond valence sum calculations for all five structures ([PDF](#))

Accession Codes

CCDC [2102482–2102485](#) and [2103588](#) contain the supplementary crystallographic data for this paper. These data can be obtained free of charge via www.ccdc.cam.ac.uk/data_request/cif, or by emailing data_request@ccdc.cam.ac.uk, or by contacting The Cambridge Crystallographic Data Centre, 12 Union Road, Cambridge CB2 1EZ, UK; fax: +44 1223 336033.

AUTHOR INFORMATION

Corresponding Authors

Miguel A. Galindo – Departamento de Química Inorgánica, Universidad de Granada, Granada 18071, Spain;
orcid.org/0000-0003-4355-4313; Email: magalindo@ugr.es

May Nyman – Department of Chemistry, Oregon State University, Corvallis, Oregon 97331, United States;
orcid.org/0000-0002-1787-0518; Email: may.nyman@oregonstate.edu

Authors

Rachelle M. Smith – Department of Chemistry, Oregon State University, Corvallis, Oregon 97331, United States; National

Institutes of Health, Bethesda, Maryland 20852, United States

Ian Colliard – Department of Chemistry, Oregon State University, Corvallis, Oregon 97331, United States

Mehran Amiri – Department of Chemistry, Oregon State University, Corvallis, Oregon 97331, United States

Complete contact information is available at:
<https://pubs.acs.org/10.1021/acs.cgd.1c01385>

Notes

Disclaimer: This article was prepared while R.M.S. was employed at the Oregon State University. The opinions expressed in this article are the authors' own and do not reflect the view of the National Institutes of Health, the Department of Health and Human Services, or the United States government.

The authors declare no competing financial interest.

ACKNOWLEDGMENTS

This study was supported by the U.S. Department of Energy, Office of Basic Energy Sciences, Division of Materials Sciences and Engineering, under the award DE SC0010802 (OSU), Spanish MINECO (CTQ2017-89311-P), Spanish MICIU (Salvador Madariaga Program, Ref. PRX19/00290), and the University of Granada (A-FQM-465-UGR18). We thank CBMM, Araxá, Minas Gerais, Brazil for the generous gift of hydrous niobia. We acknowledge the Murdock Charitable Trust (grant SR-2017297) for acquisition of the single-crystal X-ray diffractometer. M.A.G. thanks the Corvallis City Hall (Oregon, US) for the Cloverland Park Open Office facilities.

REFERENCES

- (1) New, S. Y.; Lee, S. T.; Su, X. D. DNA-Templated Silver Nanoclusters: Structural Correlation and Fluorescence Modulation. *Nanoscale* **2016**, *8*, 17729–17746.
- (2) Clever, G. H.; Shionoya, M. Metal–Base Pairing in DNA. *Coord. Chem. Rev.* **2010**, *254*, 2391–2402.
- (3) Wang, W.; Chen, S.; An, B.; Huang, K.; Bai, T.; Xu, M.; Bellot, G.; Ke, Y.; Xiang, Y.; Wei, B. Complex Wireframe DNA Nanostructures from Simple Building Blocks. *Nat. Commun.* **2019**, *10*, 1–8.
- (4) Schmidbaur, H.; Schier, A. Argentophilic Interactions. *Angew. Chem., Int. Ed.* **2015**, *54*, 746–784.
- (5) Jash, B.; Müller, J. Metal-Mediated Base Pairs: From Characterization to Application. *Chem. – Eur. J.* **2017**, *23*, 17166–17178.
- (6) Polonius, F. A.; Müller, J. An Artificial Base Pair, Mediated by Hydrogen Bonding and Metal-Ion Binding. *Angew. Chem., Int. Ed.* **2007**, *46*, 5602–5604.
- (7) Megger, D. A.; Fonseca Guerra, C.; Hoffmann, J.; Brutschy, B.; Bickelhaupt, F. M.; Müller, J. Contiguous Metal-Mediated Base Pairs Comprising Two Ag(I) Ions. *Chem. – Eur. J.* **2011**, *17*, 6533–6544.
- (8) Santamaría-Díaz, N.; Méndez-Arriaga, J. M.; Salas, J. M.; Galindo, M. A. Highly Stable Double-Stranded DNA Containing Sequential Silver(I)-Mediated 7-Deazaadenine/Thymine Watson–Crick Base Pairs. *Angew. Chem., Int. Ed.* **2016**, *55*, 6170–6174.
- (9) Méndez-Arriaga, J. M.; Maldonado, C. R.; Dobado, J. A.; Galindo, M. A. Silver(I)-Mediated Base Pairs in DNA Sequences Containing 7-Deazaguanine/Cytosine: Towards DNA with Entirely Metallated Watson–Crick Base Pairs. *Chem. – Eur. J.* **2018**, *24*, 4583–4589.
- (10) Toomey, E.; Xu, J.; Vecchioni, S.; Rothschild, L.; Wind, S.; Fernandes, G. E. Comparison of Canonical versus Silver(I)-Mediated Base-Pairing on Single Molecule Conductance in Polycytosine DsDNA. *J. Phys. Chem. C* **2016**, *120*, 7804–7809.

- (11) Kondo, J.; Tada, Y.; Dairaku, T.; Hattori, Y.; Saneyoshi, H.; Ono, A.; Tanaka, Y. A Metallo-DNA Nanowire with Uninterrupted One-Dimensional Silver Array. *Nat. Chem.* **2017**, *9*, 956–960.
- (12) Lippert, B.; Sanz Miguel, P. J. The Renaissance of Metal-Pyrimidine Nucleobase Coordination Chemistry. *Acc. Chem. Res.* **2016**, *49*, 1537–1545.
- (13) Linares, F.; García-Fernández, E.; López-Garzón, F. J.; Domingo-García, M.; Orte, A.; Rodríguez-Díéguez, A.; Galindo, M. A. Multifunctional Behavior of Molecules Comprising Stacked Cytosine–AgI–Cytosine Base Pairs; towards Conducting and Photoluminescence Silver-DNA Nanowires. *Chem. Sci.* **2019**, *10*, 1126–1137.
- (14) Mistry, L.; El-Zubir, O.; Pope, T.; Waddell, P. G.; Wright, N.; Hofer, W. A.; Horrocks, B. R.; Houlton, A. Silver–Cytidine Coordination Polymer: Electrical Properties, Modulating Intrachain Ag–Ag Distance, and MOF–Nanosheet Transformation. *Cryst. Growth Des.* **2021**, *21*, 4398–4405.
- (15) Mistry, L.; El-Zubir, O.; Dura, G.; Clegg, W.; Waddell, P. G.; Pope, T.; Hofer, W. A.; Wright, N. G.; Horrocks, B. R.; Houlton, A. Addressing the Properties of “Metallo-DNA” with a Ag(I)-Mediated Supramolecular Duplex. *Chem. Sci.* **2019**, *10*, 3186–3195.
- (16) Terrón, A.; Moreno-Vachano, B.; Bauzá, A.; García-Raso, A.; Fiol, J. J.; Barceló-Olivier, M.; Molins, E.; Frontera, A. X-Ray Crystal Structure of a Metalled Double-Helix Generated by Infinite and Consecutive C*–AgI–C* (C*:N1-Hexylcytosine) Base Pairs through Argentophilic and Hydrogen Bond Interactions. *Chem. – Eur. J.* **2017**, *23*, 2103–2108.
- (17) Pope, M. *Heteropoly and Isopoly Oxometalates*; Springer-Verlag: Berlin Heidelberg, 1983.
- (18) Blazevic, A.; Rompel, A. The Anderson–Evans Polyoxometalate: From Inorganic Building Blocks via Hybrid Organic–Inorganic Structures to Tomorrows “Bio-POM.”. *Coord. Chem. Rev.* **2016**, *307*, 42–64.
- (19) Stuckart, M.; Monakhov, K. Y. Polyoxometalates as Components of Supramolecular Assemblies. *Chem. Sci.* **2019**, *10*, 4364–4376.
- (20) Yan, J.; Gong, K.; Xue, X.; He, X.; Zhao, C.; Han, Z.; Yu, H. Two Layerlike Supramolecular Assemblies Based on B-Anderson-Type Polyanionic Clusters and Their Adsorption Property. *Eur. J. Inorg. Chem.* **2014**, *2014*, 5969–5976.
- (21) Martin, N. P.; Nyman, M. Directional Bonding in Decaniobate Inorganic Frameworks. *Angew. Chem., Int. Ed.* **2021**, *60*, 954–960.
- (22) Nohra, B.; El Moll, H.; Rodriguez Albelo, L. M.; Mialane, P.; Marrot, J.; Mellot-Draznieks, C.; O’Keeffe, M.; Ngo Biboum, R.; Lemaire, J.; Keita, B.; Nadjo, L. Polyoxometalate-Based Metal Organic Frameworks (POMOFs): Structural Trends, Energetics, and High Electrocatalytic Efficiency for Hydrogen Evolution Reaction. *J. Am. Chem. Soc.* **2011**, *133*, 13363–13374.
- (23) Du, D.-Y.; Qin, J.-S.; Li, S.-L.; Su, Z.-M.; Lan, Y.-Q. Recent Advances in Porous Polyoxometalate-Based Metal–Organic Framework Materials. *Chem. Soc. Rev.* **2014**, *43*, 4615–4632.
- (24) Wang, D.; Liu, L.; Jiang, J.; Chen, L.; Zhao, J. Polyoxometalate-Based Composite Materials in Electrochemistry: State-of-the-Art Progress and Future Outlook. *Nanoscale* **2020**, *12*, 5705–5718.
- (25) Vilà-Nadal, L.; Cronin, L. Design and Synthesis of Polyoxometalate-Framework Materials from Cluster Precursors. *Nat. Rev. Mater.* **2017**, *2*, 1–15.
- (26) Bonhomme, F.; Larentzos, J. P.; Alam, T. M.; Maginn, E. J.; Nyman, M. Synthesis, Structural Characterization, and Molecular Modeling of Dodecaniobate Keggin Chain Materials. *Inorg. Chem.* **2005**, *44*, 1774–1785.
- (27) Streb, C.; Tsunashima, R.; MacLaren, D. A.; McGlone, T.; Akutagawa, T.; Nakamura, T.; Scandurra, A.; Pignataro, B.; Gadegaard, N.; Cronin, L. Supramolecular Silver Polyoxometalate Architectures Direct the Growth of Composite Semiconducting Nanostructures. *Angew. Chem., Int. Ed.* **2009**, *48*, 6490–6493.
- (28) Huang, R.-W.; Xu, Q.-Q.; Lu, H.-L.; Guo, X.-K.; Zang, S.-Q.; Gao, G.-G.; Tang, M.-S.; Mak, T. C. W. Self-Assembly of an Unprecedented Polyoxomolybdate Anion [Mo₂₀O₆₆]¹²⁻ in a Giant Peanut-like 62-Core Silver-Thiolate Nanocluster. *Nanoscale* **2015**, *7*, 7151–7154.
- (29) Wang, Z.; Sun, Y.-M.; Qu, Q.-P.; Liang, Y.-X.; Wang, X.-P.; Liu, Q.-Y.; Kurmoo, M.; Su, H.-F.; Tung, C.-H.; Sun, D. Enclosing Classical Polyoxometallates in Silver Nanoclusters. *Nanoscale* **2019**, *11*, 10927–10931.
- (30) Qiao, J.; Shi, K.; Wang, Q.-M. A Giant Silver Alkynyl Cage with Sixty Silver(I) Ions Clustered around Polyoxometalate Templates. *Angew. Chem., Int. Ed.* **2010**, *49*, 1765–1767.
- (31) Kurasawa, M.; Arisaka, F.; Ozeki, T. Asymmetrically Fused Polyoxometalate–Silver Alkynide Composite Cluster. *Inorg. Chem.* **2015**, *54*, 1650–1654.
- (32) Ono, A.; Cao, S.; Togashi, H.; Tashiro, M.; Fujimoto, T.; Machinami, T.; Oda, S.; Miyake, Y.; Okamoto, I.; Tanaka, Y. Specific Interactions between Silver(I) Ions and Cytosine–Cytosine Pairs in DNA Duplexes. *Chem. Commun.* **2008**, *39*, 4825–4827.
- (33) Bošnjaković-Pavlović, N.; Spasojević-de Biré, A.; Tomaz, I.; Bouhmaida, N.; Avecilla, F.; Mičić, U. B.; Pessoa, J. C.; Ghermani, N. E. Electronic Properties of a Cytosine Decavanadate: Toward a Better Understanding of Chemical and Biological Properties of Decavanadates. *Inorg. Chem.* **2009**, *48*, 9742–9753.
- (34) Sánchez-Lara, E.; Treviño, S.; Sánchez-Gaytán, B. L.; Sánchez-Mora, E.; Eugenia Castro, M.; Meléndez-Bustamante, F. J.; Méndez-Rojas, M. A.; González-Vergara, E. Decavanadate Salts of Cytosine and Metformin: A Combined Experimental-Theoretical Study of Potential Metallodrugs against Diabetes and Cancer. *Front. Chem.* **2018**, *6*, 402.
- (35) Wu, P.; Wang, Y.; Huang, B.; Xiao, Z. Anderson-Type Polyoxometalates: From Structures to Functions. *Nanoscale* **2021**, *13*, 7119–7133.
- (36) Gumerova, N. I.; Roller, A.; Rompel, A. [Ni(OH)₃W₆O₁₈(OCH₂)₃CCH₂OH]⁴⁺: The First Tris-Functionalized Anderson-Type Heteropolytungstate. *Chem. Commun.* **2016**, *52*, 9263–9266.
- (37) Lin, C.-G.; Chen, W.; Long, D.-L.; Cronin, L.; Song, Y.-F. Step-by-Step Covalent Modification of Cr-Templated Anderson-Type Polyoxometalates. *Dalton Trans.* **2014**, *43*, 8587–8590.
- (38) Song, Y. F.; McMillan, N.; Long, D. L.; Thiel, J.; Ding, Y.; Chen, H.; Gadegaard, N.; Cronin, L. Design of Hydrophobic Polyoxometalate Hybrid Assemblies beyond Surfactant Encapsulation. *Chem. – Eur. J.* **2008**, *14*, 2349–2354.
- (39) Day, V. W.; Klemparer, W. G.; Maltbie, D. J. Where are the protons in H₃V₁₀O₂₈³⁻? *J. Am. Chem. Soc.* **1987**, *109*, 2991–3002.
- (40) Kojima, T.; Antonio, M. R.; Ozeki, T. Solvent-Driven Association and Dissociation of the Hydrogen-Bonded Protonated Decavanadates. *J. Am. Chem. Soc.* **2011**, *133*, 7248–7251.
- (41) Crans, D. C.; Gambino, D.; Etcheverry, S. B. Vanadium Science: Chemistry, Catalysis, Materials, Biological and Medicinal Studies. *New J. Chem.* **2019**, *43*, 17535–17537.
- (42) Aureliano, M. Decavanadate: A Journey in a Search of a Role. *Dalton Trans.* **2009**, *42*, 9093–9100.
- (43) Treviño, S.; González-Vergara, E. Metformin-Decavanadate Treatment Ameliorates Hyperglycemia and Redox Balance of the Liver and Muscle in a Rat Model of Alloxan-Induced Diabetes. *New J. Chem.* **2019**, *43*, 17850–17862.
- (44) Samart, N.; Arhouma, Z.; Kumar, S.; Murakami, H. A.; Crick, D. C.; Crans, D. C. Decavanadate Inhibits Mycobacterial Growth More Potently than Other Oxovanadates. *Front. Chem.* **2018**, *6*, 519.
- (45) Chatkon, A.; Chatterjee, P. B.; Sedgwick, M. A.; Haller, K. J.; Crans, D. C. Counterion Affects Interaction with Interfaces: The Antidiabetic Drugs Metformin and Decavanadate. *Eur. J. Inorg. Chem.* **2013**, *2013*, 1859–1868.
- (46) Aureliano, M.; Crans, D. C. Decavanadate (V₁₀O²⁸⁶⁻) and Oxovanadates: Oxometalates with Many Biological Activities. *J. Inorg. Biochem.* **2009**, *103*, 536–546.
- (47) Krivosudský, L.; Roller, A.; Rompel, A. Tuning the Interactions of Decavanadate with Thaumatin, Lysozyme, Proteinase K and Human Serum Proteins by Its Coordination to a Pentaquaacobalt(II) Complex Cation. *New J. Chem.* **2019**, *43*, 17863–17871.

- (48) An, H.; Li, Y.; Wang, E.; Xiao, D.; Sun, C.; Xu, L. Self-Assembly of a Series of Extended Architectures Based on Polyoxometalate Clusters and Silver Coordination Complexes. *Inorg. Chem.* **2005**, *44*, 6062–6070.
- (49) McGlone, T.; Thiel, J.; Streb, C.; Long, D. L.; Cronin, L. An Unprecedented Silver-Decavanadate Dimer Investigated Using Ion-Mobility Mass Spectrometry. *Chem. Commun.* **2012**, *48*, 359–361.
- (50) Kulikov, V.; Meyer, G. A New Strategy for the Synthetic Assembly of Inorganic-Organic Silver(I)-Polyoxometalate Hybrid Structures Employing Noncovalent Interactions between Theobromine Ligands. *Cryst. Growth Des.* **2013**, *13*, 2916–2927.
- (51) Nyman, M. Polyoxoniobate Chemistry in the 21st Century. *Dalton Trans.* **2011**, *40*, 8049–8058.
- (52) Perloff, A. Crystal Structure of Sodium Hexamolybdochromate(III) Octahydrate, $\text{Na}_3(\text{CrMo}_6\text{O}_{24}\text{H}_6)\cdot 8\text{H}_2\text{O}$. *Inorg. Chem.* **1970**, *9*, 2228–2239.
- (53) Domaille, P. J. The 1- and 2-Dimensional Tungsten-183 and Vanadium-51 NMR Characterization of Isopolymetalates and Heteropolymetalates. *J. Am. Chem. Soc.* **2002**, *106*, 7677–7687.
- (54) Sures, D.; Segado, M.; Bo, C.; Nyman, M. Alkali-Driven Disassembly and Reassembly of Molecular Niobium Oxide in Water. *J. Am. Chem. Soc.* **2018**, *140*, 10803–10813.
- (55) Fullmer, L. B.; Mansergh, R. H.; Zakharov, L. N.; Keszler, D. A.; Nyman, M. Nb_2O_5 and Ta_2O_5 Thin Films from Polyoxometalate Precursors: A Single Proton Makes a Difference. *Cryst. Growth Des.* **2015**, *15*, 3885–3892.
- (56) SAINT Plus; 8.34a; Brucker Anal. X-Rays Syst.: Madison, WI2013e.
- (57) Sheldrick, G. M. SADABS, Bruker-Siemens Area Detect. *Absorpt. Other Correct.* Version 2008/12008.
- (58) Sheldrick, G. M. SHELXT - Integrated Space-Group and Crystal-Structure Determination. *Acta Crystallogr. Sect. A Found. Crystallogr.* **2015**, *71*, 3–8.
- (59) Sheldrick, G. M. A Short History of SHELX. *Acta Crystallogr., Sect. A: Found. Crystallogr.* **2008**, 112–122.
- (60) Dolomanov, O. V.; Bourhis, L. J.; Gildea, R. J.; Howard, J. A. K.; Puschmann, H. OLEX2: A Complete Structure Solution, Refinement and Analysis Program. *J. Appl. Crystallogr.* **2009**, *42*, 339–341.
- (61) Liu, H.; Shen, F.; Haruehanroengra, P.; Yao, Q.; Cheng, Y.; Chen, Y.; Yang, C.; Zhang, J.; Wu, B.; Luo, Q.; Cui, R.; Li, J.; Ma, J.; Sheng, J.; Gan, J. A DNA Structure Containing AgI-Mediated G:G and C:C Base Pairs. *Angew. Chem., Int. Ed.* **2017**, *56*, 9430–9434.
- (62) Müller, J. Nucleic Acid Duplexes with Metal-Mediated Base Pairs and Their Structures. *Coord. Chem. Rev.* **2019**, *393*, 37–47.
- (63) Nakamura, S.; Ozeki, T. Hydrogen-Bonded Aggregates of Protonated Decavanadate Anions in Their Tetraalkylammonium Salts. *J. Chem. Soc., Dalton Trans.* **2001**, *4*, 472–480.
- (64) Villa, E. M.; André Ohlin, C.; Balogh, E.; Anderson, T. M.; Nyman, M. D.; Casey, W. H. Reaction Dynamics of the Decaniobate Ion $[\text{HxNb}_{10}\text{O}_{28}]^{(6-x)-}$ in Water. *Angew. Chem., Int. Ed.* **2008**, *47*, 4844–4846.
- (65) Xiong, Y.; Washio, I.; Chen, J.; Sadilek, M.; Xia, Y. Trimeric Clusters of Silver in Aqueous AgNO_3 Solutions and Their Role as Nuclei in Forming Triangular Nanoplates of Silver. *Angew. Chem., Int. Ed.* **2007**, *46*, 4917–4921.
- (66) Moussa, J.; Boubekeur, K.; Amouri, H. Self-Assembly of 1-D Coordination Polymers Using Organometallic Linkers and Exhibiting Argentophilic Interactions $\text{AgI}\cdots\text{AgI}$. *Eur. J. Inorg. Chem.* **2005**, *2005*, 3808–3810.

□ Recommended by ACS

DNA-Mediated Three-Dimensional Assembly of Hollow Au-Ag Alloy Nanocages as Plasmonic Crystals

Eli Sutter, Peter Sutter, et al.

JULY 22, 2020

ACS APPLIED NANO MATERIALS

READ ▶

Spectrum-Quantified Morphological Evolution of Enzyme-Protected Silver Nanotriangles by DNA-Guided Postshaping

Junyao Li, Zihui Dai, et al.

NOVEMBER 10, 2019

JOURNAL OF THE AMERICAN CHEMICAL SOCIETY

READ ▶

Unified Etching and Protection of Faceted Silver Nanostructures by DNA Oligonucleotides

Shengqiang Hu, Juewen Liu, et al.

APRIL 22, 2019

THE JOURNAL OF PHYSICAL CHEMISTRY C

READ ▶

Noncanonical Head-to-Head Hairpin DNA Dimerization Is Essential for the Synthesis of Orange Emissive Silver Nanoclusters

Pratik Shah, Seong Wook Yang, et al.

JUNE 11, 2020

ACS NANO

READ ▶

Get More Suggestions >